Cu-Sn Bimetallic Catalyst for Selective Aqueous Electroreduction of CO2 to CO

Article

Cu-Sn Bimetallic Catalyst for Selective Aqueous Electroreduction of CO2 to CO

Saad Sarfraz, Angel T Garcia-Esparza, Abdesslem Jedidi, Luigi Cavallo, and Kazuhiro Takanabe

ACS Catal., **Just Accepted Manuscript** • DOI: 10.1021/acscatal.6b00269 • Publication Date (Web): 23 Mar 2016

Cu-Sn Bimetallic Catalyst for Selective Aqueous Electroreduction of CO_2 to CO

*Saad Sarfraz[‡], Angel T. Garcia-Esparza[‡], Abdesslem Jedidi, Luigi Cavallo, and Kazuhiro Takanabe**

King Abdullah University of Science and Technology (KAUST), KAUST Catalysis Center (KCC), and Physical Sciences and Engineering Division (PSE), Thuwal, 23955-6900, Saudi Arabia.

ABSTRACT. We report a selective and stable electrocatalyst utilizing non-noble metals consisting of Cu and Sn for the efficient and selective reduction of CO_2 to CO over a wide potential range. The bimetallic electrode was prepared through the electrodeposition of Sn species on the surface of oxide-derived copper (OD-Cu). The Cu surface, when decorated with an optimal amount of Sn, resulted in a Faradaic efficiency (FE) for CO greater than 90% and a current density of −1.0 mA cm^{-2} at −0.6 V vs. RHE, compared to the CO FE of 63% and −2.1 mA cm^{-2} for OD-Cu. Excess Sn on the surface caused H_2 evolution with a decreased current density. X-ray diffraction (XRD) suggests the formation of Cu-Sn alloy. Auger electron spectroscopy of the sample surface exhibits zero-valent Cu and Sn after the electrodeposition step. Density functional theory (DFT) calculations show that replacing a single Cu atom with a Sn atom leaves the d-band orbitals mostly unperturbed, signifying no dramatic shifts in the bulk electronic structure. However, the Sn atom discomposes the multi-fold sites on pure Cu,

disfavoring the adsorption of H and leaving the adsorption of CO relatively unperturbed. Our catalytic results along with DFT calculations indicate that the presence of Sn on reduced OD-Cu diminishes the hydrogenation capability—i.e., the selectivity towards H_2 and HCOOH—while hardly affecting the CO productivity. While the pristine monometallic surfaces (both Cu and Sn) fail to selectively reduce CO_2, the Cu-Sn bimetallic electrocatalyst generates a surface that inhibits adsorbed H*, resulting in improved CO FE. This study presents a strategy to provide a low-cost non-noble metals that can be utilized as a highly selective electrocatalyst for the efficient aqueous reduction of CO_2.

KEYWORDS. electrocatalysis; CO_2 reduction; bimetallic catalyst; artificial photosynthesis; density functional theory

1. Introduction

The concept of CO_2 conversion through renewable energy poses an excellent strategy to not only mitigate excess CO_2 levels in the atmosphere but also produce valuable compounds.[1] To date, several approaches are being studied for CO_2 conversion, ranging from CO_2 sequestration and storage to the use of electrochemical, photocatalytic, or direct catalytic conversions.[2,3] Electrocatalytic reduction of CO_2 is a promising process to create valuable chemicals owing to its ambient operating conditions, scalability, and reasonably high reaction rates.[4-5] Existing noble metal electrocatalysts for CO_2 reduction have shown favorable results to generate CO and formic acid (HCOOH) at relatively low overpotentials. Au (−0.35 V vs. RHE, 2 to 4 mA cm^{-2}),[6] Pd nanoparticles (−0.05 V vs. RHE, 2 mA cm^{-2})[7] and nanoporous Ag (−0.5 V vs. RHE, 9 mA cm^{-2})[8] are highly active. Similarly, Hahn *et al.* demonstrated that alloying Au with Pd increases

the FE to formate with pure Au and Pd catalysts.[9] Kortlever et al. used Pd-Pt alloy nanoparticles for selective formic acid generation (FE ~88%) at low overpotential at −0.4 V vs. RHE.[10] However, their implementation at an industrial scale is unsustainable and has limitations owing to the scarcity of noble metals.[7-10]

Previous studies by Hori and coworkers have demonstrated that Cu is unique compared with other metals in its ability to produce hydrocarbons at potentials more negative than −1 V vs RHE.[11] Nevertheless, the large overpotential renders the process inefficient. More recently, Li and Kanan showed that oxide-derived copper (OD-Cu), when reduced electrochemically, can produce a mixture of CO and HCOOH from CO_2 at moderate potentials (−0.5 V vs. RHE), with reasonable FE towards CO (~40% FE at 2.5 mA cm^{-2}).[12] This work demonstrated a significant difference against polycrystalline copper, which produces mostly H_2 at similar overpotentials (more positive than −0.9 V vs. RHE).[13] This improvement in CO FE has been attributed to the formation of active sites that bind CO strongly. Such sites can be produced from the electrochemical reduction of the oxides of Cu to the metallic state.[14] Subsurface oxides may exist and can alter the binding nature of the sites for CO_2 reduction, enhancing the selectivity at low overpotentials.[15,16] Similarly, electrochemically reduced PbO_2 has shown nearly ~100% FE towards CO_2 reduction to formate at −0.75 V vs. RHE with a formate specific current density of 0.1 mA cm^{-2}.[17] MoS_2 is another non-noble catalyst that has shown high activity for CO_2 reduction (98% CO FE with 65 mA cm^{-2} at −0.76 V vs. RHE) in 4% ionic liquid, 1-ethyl-3-methylimidazolium tetrafluoroborate (EMIM-BF_4).[18] Rosenthal and co-workers have reported a generalized strategy for the electrodeposition of inexpensive electrocatalytic films from triflate salts of Bi^{3+}, Sb^{3+}, Sn^{2+}, and Pb^{2+} in organic media.[19-21] When the Bi-based electrodes are used for electrochemical CO_2 reduction in acetonitrile with a low overpotential of 250 mV, the

electrocatalysts are highly selective towards CO only when an appropriate ionic liquid is present in the system (1-ethyl-3-methylimidazolium hexafluorophosphate [EMIM]PF_6, or 1-butyl-3-methylimidazolium hexafluorophosphate [BMIM]PF_6, with an average 81% CO FE with 25-30 mA cm^{-2}).[19-21] These seminal studies have thus clearly indicated that non-noble catalysts have the capability to compete with noble metals for CO_2 reduction.

As for a rationalization of the experimental evidences, DFT calculations have suggested a scaling relationship between the adsorption strengths of CO and COOH on the catalyst and the overpotential for CO_2 reduction.[22] A trend for the conversion efficiency of CO_2 to COOH* and CO* to CHO (as usual, the * indicates adsorbed species) as a function of the metal–adsorbate bond strength shows that Cu is at the top of the volcano plot among various transition mono-metals.[16] To break the scaling trends, one strategy may be to use alloys that can decouple the binding energies for CO and CHO adsorptions, potentially lowering overpotentials and improving product selectivity.[22,23] Using the aforementioned method, we reported a bimetallic Cu-In electrocatalyst that achieved CO FE of ~85% (−0.6 V vs. RHE, ≈ −0.75 mA cm^{-2}).[24,25] As for alloying Cu with other metals, Watanabe et al. reported the synergistic effect of the Cu alloys with various metals, among which Sn ($Cu_{57}Sn_{43}$) produced CO (~16% FE) compared with pristine Cu (0%) and Sn (0%) at the same reaction condition.[26] Separately, Hori and coworkers reported that the reduction of CO_2 on an Sn electrode primarily leads to the production of formate (~88.4 % FE) at high overpotential (−1.1 V vs. RHE).[27,28] At a moderate potential (−0.6 V vs. RHE), Sn metal mostly produces H_2 with HCOOH (~12% FE) and CO (~2% FE).[25] In contrast, oxidized Sn dendrites exhibited ~30 to 50% FE towards formate at −0.66 V vs. RHE, together with 20% FE to CO.[28] Electrodeposited SnO_x thin films on an Sn sheet substrate produced formate with a 40% FE yet with an increased selectivity towards CO (60% FE at −0.7

V vs. RHE).[29] This increased selectivity, compared with pristine Sn, was ascribed to the surface oxide species, which may stabilize the CO_2^- intermediate.[28,29] Consistently, H_2 was favored when more positive potentials than −0.7 V vs. RHE were applied to the Sn surface but with lower current densities due to the high overpotential to catalyze the hydrogen evolution reaction on metallic Sn.

Based on this background, we decided to explore the incorporation of a secondary metal with Cu that has a high overpotential for H_2 evolution.[30,31] Herein, we employed Sn as an inexpensive and abundant metal along with OD-Cu to prepare a highly selective catalyst for CO_2 reduction to CO. We systematically and carefully electrodeposit Sn species on reduced OD-Cu surfaces, varying monometallic Cu to bimetallic Cu-Sn and further to monometallic Sn (on Cu). Our results show that the Cu-Sn bimetallic surface exhibits highly selective and stable performance, resulting in >90% FE towards CO for at least 14 h of CO_2 reduction reaction at −0.6 V vs. RHE. A strategy to design selective surfaces is presented, in which the H-binding sites are perturbed to diminish the competitive H_2 evolution without altering the activity towards CO_2 reduction.

2. Experimental and theoretical methods

Materials. Cu sheets of 0.2 mm thickness (99.9% purity) and Sn sheets of 0.1 mm thickness (99.9% purity) were purchased from Nilaco Corporation, Japan. An Ag/AgCl reference electrode saturated in KCl was purchased from BAS Corporation, Japan. $SnCl_2 \cdot 2H_2O$ (99.995% trace metals basis), $KHCO_3$ (99.99%), KOH (99.99% trace metals basis), HNO_3 (ACS reagent, assay ≥ 69%), HCl (ACS reagent, assay 36.5–38.0%), and Cu-rich $Cu_{84}Sn_5$ bronze powder at 200 mesh were obtained from Sigma Aldrich. High-purity CO_2 (99.9999%) gas was acquired from AHG industrial gases, Saudi Arabia.

Electrochemistry. A BioLogic© VMP3 potentiostat was used for all electrochemical measurements including electrodeposition and CO_2 electrolysis. A micro gas chromatograph (μGC, T-3000) from SRA-Instruments was used with a 5 Å MolSieve column and a thermal conductivity detector for the characterization of gaseous compounds. Liquid products were quantified using high-performance liquid chromatography (HPLC) from Agilent Technologies with an ICE-Coregel 87-H3 column equipped with a 1260 Infinity Variable Wavelength Detector and a 1260 Infinity Refractive Index Detector for the detection of HCOOH and alcohols, respectively. A customized airtight, two-compartment, three-electrode cell was utilized with our samples as the working electrode, and Pt was isolated as the counter electrode. Ag/AgCl (saturated KCl) was used as the reference electrode. The electrochemical reduction of CO_2 was carried out using a 0.1 M $KHCO_3$ solution (pH 6.8) under high stirring. The electrolyte was saturated with CO_2 for at least 30 min before the start of each CO_2 reduction, and the flowrate of CO_2 was maintained at 10 mL min^{-1} for all experiments. All potentials for CO_2 reduction are reported with respect to the reversible hydrogen electrode (RHE).

Preparation of OD-Cu. The pristine Cu sheet (0.2 mm thickness, 99.9%) was cut into 1 × 2 cm^2 plates and washed with water before sonicating for 3 min in acetone. An etching solution of 2 M HNO_3 was used to further clean the sheets from surface impurities. Copper plates were washed with nitric acid for 3 min under sonication and then washed at least three times with Milli-Q water. The etched copper plates were dried by blowing N_2 gas after removal from water. The plates were then placed vertically in alumina crucibles and heated at 400 °C for 2 h in a muffle furnace with static air under a ramping rate of 200 °C h^{-1}.

Preparation of Sn. Sn metal sheet (0.1 mm thickness, 99.9%) was purchased from Nilaco Corporation (Japan) and cut into 3 × 1 cm^2 sheets. The sheets were washed with acetone and

water before begin washed with 1 M HCl for a few seconds. When used as an anode in a two-electrode system, an active surface area of 3.0 cm^2 for Sn was maintained for each electrodeposition protocol. The Sn sheet used as a substrate for the electroplating of Sn was pretreated with 2 M HNO_3 for 2 min, rinsed with Milli-Q water and dried with N_2 gas.

Electrodeposition of Sn on OD-Cu. Sn was electrodeposited on OD-Cu electrodes in a two-electrode cell with Sn sheet as the anode. The electrolyte consisted of a solution of 0.05 M $SnCl_2 \cdot 2H_2O$ with 2 M KOH. Electrodeposition was carried out at a constant potential of −0.5 V vs. Sn while varying the passing charge density either on pre-reduced OD-Cu (0.1, 0.3, 0.5, 0.75, 1.5, and 2.0 C cm^{-2}) or pristine OD-Cu (1.0, 4.0, 6.3, 8.0, 10.0 and 15.0 C cm^{-2}). The pre-reduction of OD-Cu, prior to Sn electrodeposition, was conducted at −0.6 V vs. RHE for 1 h followed by −0.8 V vs. RHE for 1 h in CO_2 reduction solution. The deposited amount determined by inductively coupled plasma (ICP) measurements was also used to report in the unit of μmol cm^{-2}.

Preparation of electrode made of commercial Cu-Sn alloy particles. $Cu_{84}Sn_5$ powder was annealed in a tube furnace under N_2 at 1100 °C for 5 h using an alumina boat, to form a rather flat bulk electrode of the alloy. The cooling step was performed under inert conditions, and the sample was exposed to air after reaching room temperature. A copper wire was soldered using indium to create a low-resistance ohmic contact with the alloy electrode, which was later sealed with epoxy to cover all connections, exposing only a well-defined active surface.

Characterization of materials. ICP measurements were taken using a Varian 720-ES equipped with a charge coupled device (CCD) detector. All samples were digested in concentrated HNO_3 using a microwave digestion system. Samples were diluted with 1% HNO_3 prior to all measurements. A standard error of ±2 ppm was calculated based on the average of the

experimental standard deviations for each set of measurements. Sn standard solution (1000 ppm) was obtained from Inorganic Ventures and diluted for the calibration measurements. X-ray diffraction (XRD) patterns were obtained using a Bruker D8 Advanced A25 diffractometer with a Cu X-ray tube (Cu–Kα; λ = 0.154 nm). The diffractometer operating conditions were 40 mA at 40 mV. X-ray photoelectron spectroscopy (XPS) was performed using a 3400 KRATOS AMICUS/ESCA with an unmonochromatized Al-anode Kα X-ray source (1486.6 eV) operated at 15 mA and 10 kV (~ 1×10^{-7} Pa). The binding energies were calibrated using the adventitious C 1s spectra with a reported binding energy of 284.8 eV, and the associated error was estimated to be at least ±0.2 eV to ±0.3 eV.[32] Scanning electron microscopy (SEM) images were obtained at 5 keV using a NovaNano scanning electron microscope from FEI.

Computational details. Electronic structure calculations based on DFT were performed using the revised Perdew–Burke–Ernzerhof (revPBE) exchange-correlation functional as implemented in VASP.[33-36] Plane–wave basis sets (with a kinetic energy cutoff of 500 eV)[37] describe the valence electrons: 11 electrons of Cu ($3d^{10}4s^{1}$) and three electrons of Sn ($5s^{2}5p^{2}$). We employed a 0.1 eV smearing of the Fermi level and (8×8×8) K-points for bulk calculations and (4×4×1) for surfaces. The core electrons were replaced by projector augmented wave (PAW) pseudopotentials.[38,39] The relaxation of the atomic positions in the supercell occurred until the energy differences were smaller than 0.01 eV $Å^{-1}$. With this setup, we simulated the electronic structure of Cu/Sn alloys, the substitution of one Cu atom by a Sn atom in Cu nanoparticles, and the same substitution on regular Cu surfaces.

The electronic structure of the Cu-Sn alloy was investigated in the bulk structure with different concentrations of tin (25, 45, 50 and 75%). Special-quasi-random (SQS) structures from literature were used to model alloys with Sn contents of 25, 50 and 75%.[40,41] We used a 2×2×2

(32 atoms) fcc supercell with a lattice constant of 3.62 Å.[40] The calculations show only one stable structure corresponding to $Cu_{75}Sn_{25}$; the two other structures become completely distorted after optimization. We also investigated two experimental structures of the well-defined Cu_3Sn (25 at.% Sn) and Cu_6Sn_5 (45 at.% Sn) alloys.[42] Icosahedral and cuboctrahedral Cu_{55} nanoparticles[43,44] were placed in a repeating cubic box with an edge large enough to prevent interactions between the images (more than 10 Å between successive images). Finally, the (100), (111) and (211) Cu surfaces were modeled with slabs of four atomic layers. We used a p(3×3) supercell with a vacuum in the direction perpendicular to the surface of 12 Å. The modification of the surface was performed by replacing a Cu atom from the top and the second layer with a Sn atom. Adsorption of H and CO on the (100) facets was modeled with a slab of three atomic layers; the bottom layer was frozen in these calculations.

3. Results and Discussion

Electrochemical measurements

Chronoamperometry was performed on OD-Cu (Figure 1a), electrodeposited Sn on the pre-reduced OD-Cu (Figure 1b, referred to as "Cu-Sn" hereafter) and electrodeposited Sn on Sn sheet (Figure 1c) to study the reduction of CO_2 for 2 h at −0.6 V vs. RHE. H_2, CO, HCOOH, and CH_3COOH were the only detected reaction products by μGC and HPLC. The amount of Sn deposition of 3.9 μmol cm^{-2} as a result of 0.3 C cm^{-2} electrodeposition process. An induction period of max. 30 min was observed at the start of the experiments, which can be attributed to the reduction of copper or tin oxides and the filling of the dead-space volume of the electrochemical cell. After this induction period, a stable concentration profile of the products for all the electrodes was observed as the current reached steady state conditions, and the average FE

was determined at this point. From Figure 1a, FE for CO_2 reduction products (CO + HCOOH) using the OD-Cu electrode was higher (88%) than previously reported in the literature (61%).[11] See Table S1 for product comparison of different OD-Cu in the literature. Previous studies have shown a broad product distribution in CO_2 reduction with varying results for H_2, ranging from 30 to 50% FE.[12,15,45] The observed improvement in CO_2 conversion efficiency for the OD-Cu electrode in this study can be due to the careful acid pretreatment of the electrode, probably removing existing active species for H_2, and the subsequent 400 °C annealing step, in contrast to the 500 °C heat treatment previously used to build the copper oxide layers.[12,21,45,46] Next, the electrocatalytic performance of Cu-Sn exhibited a remarkably high FE towards CO, achieving > ~90% at −0.6 V (Figure 1b). A long-term stability of the Cu-Sn was observed for 14 h, which showed an initial ~95% CO FE for 6 h; subsequently decreasing to ~90%, with the H_2 FE increasing over time from ~8% to ~12%. The CO_2 electroreduction experiment using Sn plated on Sn sheet (Figure 1c) showed exclusively H_2 production without the formation of products from CO_2 reduction. A comparison of the total geometric current density as a function of the applied potential for the three materials is shown in Figure 2. The current density of Cu-Sn was lower than that of OD-Cu but larger than Sn deposited on Sn, showing that the overall activity decreased when more Sn was present on the electrode surface.

FEs for the three samples between −0.4 and −0.8 V vs. RHE are compared in Figure 3. The OD-Cu sample (Figure 3a) showed 48% CO FE at −0.4 V vs. RHE, which increases to 63% FE at −0.6 V vs. RHE and again declines to 44% FE at −0.7 V vs. RHE and 32% FE at −0.8 V vs. RHE. In contrast, HCOOH FE monotonically increased with increasing overpotential using OD-Cu, reaching 45% FE at −0.8 V vs. RHE. Minute quantities of CH_3COOH (~2% FE) were detected at −0.8 V vs. RHE. The trend of these products for OD-Cu is consistent with the

literature for copper oxide based electrodes (see Table S1).[12,15,24] In the case of Cu-Sn, more than 90% CO FE was observed throughout a broad potential range (from −0.5 to −0.8 V vs. RHE) whereas only sparse amounts of H_2 and HCOOH were observed (Figure 3b). The similar CO selectivity as a function of applied potentials suggests a consistent mechanism for CO_2 reduction in the studied potential range. The Sn deposited on Sn electrode showed exclusively H_2 evolution throughout the investigated potentials (Figure 3c). Similarly, the washed Sn sheet (without Sn deposition) predominantly produced H_2 with only small quantity of HCOOH and CO at −0.7 and −0.8 V vs. RHE (Figure S1), consistent with the literature.[13,28,45] Previously, we have shown a Cu-In electrocatalyst forming CO with 80% FE at −0.5 V vs. RHE with a 20% FE for H_2 with a current density of −0.5 mA cm^{-2}.[24] The Cu-In electrode showed almost 90% FE towards CO at −0.6 V vs. RHE; however, the stability was compromised after 4 h of CO_2 reduction, decreasing to 85% FE with a current density of –0.6 mA cm^{-2}.[24] The Cu-Sn electrocatalyst in the current study exhibited high stability with 90% CO FE at −1 mA cm^{-2} under similar potentials. Also the performance of Sn deposited on the washed Cu sheet (not OD-Cu) under similar conditions (0.5 C cm^{-2}, 0.05 M $SnCl_2$, 2 M KOH, Figure S2). Similarly to pristine Cu and Sn deposited on Sn sheet, the result indicated the preferred generation of H_2 (>98% FE, from −0.4 to −0.7 V vs. RHE) with minor amounts of CO (8% FE) and formate (10% FE) at −0.8 V vs. RHE. We note from this result that Sn deposited on OD-Cu is the only case where high CO FE was observed, suggesting that both OD-Cu and Sn are required to achieve this selectivity.

The effect of Sn on the current densities and the FEs was further explored by increasing the charge of Sn electrodeposition (Figure 4a and 4b). After electrodeposition, CO_2 reduction was performed at −0.6 and −0.8 V vs. RHE for 1 h at each potential, and the electrodes were analyzed using ICP to determine the deposited amount of Sn in the active surface. Figure 4a and

4b show a monotonic decrease in the current density with increasing amount of deposited Sn. As the amount of Sn increased to 4.4 μmol cm^{-2}, the H_2 and HCOOH FEs decreased. The optimal point in the curve was observed at 3.9 μmol cm^{-2} of Sn with a selectivity of 95% for the CO_2 reduction (90% CO FE and 5% HCOOH FE at −0.6 V vs. RHE). From 23.5 to 35.1 μmol cm^{-2}, a pronounced change was observed with a steep increase in H_2 and HCOOH generation, reaching ~68% H_2 FE and ~17% HCOOH FE for the latter concentration (−0.6 V vs. RHE, Figure 4a). This drastic change in product selectivity may be directly correlated with the fact that the deposited Sn surpassed monolayer of the OD-Cu surface. When the amount of electroplated Sn was relatively large (i.e., >23 μmol cm^{-2}) the current exhibited a 7-fold decrease, generating H_2 with >70% FE. These results were consistent with a complementary set of experiments in which we increased the electrodeposition charge for Sn on OD-Cu, without any pre-reduction step to reduce the oxidized Cu (Figure S3). We obtained similar trends as previously observed, in which increasing the electrodeposited charge to form Sn on OD-Cu resulted in decreasing current densities with increasing selectivity towards H_2 (compare Figure 4 and Figure S3). The double layer capacitance of the reduced OD-Cu sample and the Cu-Sn (6.3 C cm^{-2}) shows that Sn deposition led to slight decrease in total surface area with a factor of 0.74 (Figure S4). The loss of total current was a factor of <0.7 (0.56-0.69), suggesting that the degree of deactivation by the Sn deposition was more severe than the degree of loss in surface area. We performed CO_2 reduction at −0.6 V vs. RHE for 1 h and observed that the highest CO FE occurred at an optimal charge of 6.3 C cm^{-2}. Furthermore, when changing the applied potentials from −0.6 to −0.8 V vs. RHE (compare Figure 4a and 4b), the HCOOH FE increased in all samples, whereas the CO FE decreased (i.e., more negative than −0.7 V vs. RHE), suggesting that more negative potentials favor HCOOH, following a similar trend as previously seen with OD-Cu (Figure 3a) and

metallic Sn (Figure 3c). Figure 4a and 4b show that after 4.4 μmol cm^{-2}, the FE for H_2 increased drastically. The results in which Sn is present in quantities larger than 23 μmol cm^{-2} or the Sn electrodeposition charge was >10 C cm^{-2} imply the formation of a metallic Sn layer, blocking the underlying Cu. Hence, the electrode behavior was similar to a pristine Sn plate and Sn deposited on Sn sheet (at −0.6 V vs. RHE, ≈−0.3 mA cm^{-2}, Figure 1, Figure S1 and Figure S3). With a systematic variation of the atomic composition of the surface from monometallic Cu to bimetallic Cu-Sn and finally to monometallic Sn, we have shown that the selectivity of the electrocatalyst can be tuned from water reduction to CO_2 reduction. The Sn-modified oxide-derived Cu surface was capable of efficient and selective production of CO from aqueous CO_2; nevertheless, the monometallic sites did not exhibit such behavior.

Structural characterization

The optimal composition for the Cu-Sn electrocatalyst was used for systematic characterizations in an effort to understand the nature of the active surface. First, SEM micrographs were obtained for the Cu-Sn electrode before and after 1 h of CO_2 reduction at −0.6 V vs. RHE (Figure 5). Prior to CO_2 reduction, the Cu-Sn sample (Figure 5a) showed a rough, grain-like structure. The same Cu-Sn sample exhibited a completely transformed morphology after CO_2 reduction (Figure 5b). It was possible to observe the presence of nanocubes with measured sizes of approximately 92 ± 12 nm, which are homogeneously dispersed. Based on previous reports, Cu cubes with (100) domain surface may form upon the reduction of Cu_2O, which is consistent with the results from electrochemical[47] and photoelectrochemical protocols.[15,48] Nevertheless, the reduction of OD-Cu in carbonate electrolytes generally forms Cu

nanoparticle aggregates without defined cubic structures.[12,15] The presence of smaller particle aggregates can be observed covering the surface of the cubes (Figure 5b).

The samples produced by passing large charges of Sn electrodeposition were characterized via XRD (Figure S5). The diffractograms revealed that as the electrodeposition charge was increased, new diffractions appeared that were ascribed to metallic Sn (PDF 00-004-0673) and the formation of alloy phases ($Cu_{6.26}Sn_5$, PDF 00-047-157; and $Cu_{3.02}Sn_{0.98}$, PDF 03-065-5721); this suggests that prolonged electrodeposition formed metallic Sn structures and alloys with varying compositions, which may promote H_2 evolution. Next, a detailed XRD characterization of the optimized Cu-Sn sample before and after 1 h and 14 h of CO_2 electroreduction is presented in Figure 6. All samples showed intense metallic Cu diffractions that appeared mostly owing to the substrate at 43.5° (111) and 50.6° (110) (PDF 00-004-0836). All samples exhibited diffraction peaks that were assigned to Cu_2O at 36.7° (111) and 61.6° (220) (PDF 01-071-3645) before and after reaction. In the diffractograms presented in Figure 6, amorphous phases were observed in the region below 30° (a complete XRD spectrum from θ = 10° to 100° is presented in Figure S6). Mixtures of oxidized Sn(II) and Sn(IV) may generate amorphous structures. After electroplating Sn on reduced OD-Cu, we observed peaks at 38.9° (106) and 66.1° (227) that were attributed to the formation of SnO_2 (PDF 01-078-1063). Those diffractions remained after 1 h of electrocatalytic CO_2 reduction. Nevertheless, after 14 h of steady-state cathodic conditions, the peaks ascribed to SnO_2 were mostly absent. After the long-term stability test of the Cu-Sn sample, it was possible to observe the appearance of a new diffraction feature near 2θ = 41° ("Cu-Sn after 14 h reaction", Figure 6). The diffraction peak was attributed to the formation of a Cu-Sn alloy. The alloy composition may be in the range of $Cu_{6.26}Sn_5$, $Cu_{3.02}Sn_{0.98}$ or $(Cu_{32}Sn)_{0.12}$ (PDF 01-077-7742). Although the precise position of the

peak suggests a different d-spacing from the aforementioned alloys, it appears that the formation of the alloy under steady-state conditions for electrochemical CO_2 reduction is possible.

The catalytically active surface was analyzed by means of ex-situ XPS. The XPS spectra of the Cu 2p region are very challenging to interpret because the metallic state of Cu and Cu(I) have statistically similar binding energy values (Figure S7a).[49-55] Hence, the X-ray generated Auger spectra were recorded in the Cu $L_3M_{45}M_{45}$ region, and the results are presented in Figure 7a. The literature reports metallic Cu with a characteristic peak in the range of 918.2 to 918.6 eV; Cu_2O has a reported peak between 916.0 and 916.4 eV, and the peak for the CuO standard increases from 917.6 to 917.8 eV.[49-55] The acid-treated Cu sheet resulted in spectra similar to those previously reported in the literature for air-oxidized metallic Cu.[54,55] This oxidized layer was reported to be in the size range of 1.6 to 2.7 nm.[55] For the OD-Cu electrode after the 400 °C heat treatment ("OD-Cu before"), the Auger spectrum exhibited a broad peak at 917.7 eV, indicating the presence of Cu(II) in the surface as CuO. After performing the CO_2 reduction experiment with the OD-Cu electrode ("OD-Cu after"), the Auger spectrum was similar to Cu_2O with a peak at 916.4 eV, together with the subsequent shoulder at 918.5 eV correlating well with the kinetic energy characteristic of metallic Cu.[55,56] In contrast, the Auger spectrum for the Cu-Sn before electrocatalysis ("Cu-Sn before") indicated a similar state to the Cu sheet reference with a peak maximum at 916.4 eV and a clear shoulder at 918.4 eV ascribed to Cu_2O and Cu metal, respectively. For the Cu-Sn sample after the reaction ("Cu-Sn after"), there was a clear Auger peak at 918.3 eV, which was attributed to the existence of zero-valent Cu species. The XPS spectra for Sn 3d are shown in Figure 7b. After electroplating Sn on OD-Cu before CO_2 reduction ("Cu-Sn before"), we observed in the Sn $3d_{5/2}$ line a minor peak located at 484.9 eV, which can be attributed to zero valent Sn.[57] A similar feature can be observed in the reference

$Cu_{84}Sn_5$ alloy ("$Cu_{84}Sn_5$ Aldrich"). For "Cu-Sn after" sample, only a single Sn 3d doublet was resolved in the Cu-Sn electrode, which may be attributed to mixed-valence oxidized Sn species in the surface and resembles the spectra of an air-oxidized Sn surface.[58] The spectrum resembles that of commercially-available CuSn alloy particles, which should possess zero-valent Sn species in the matrix of metallic Cu. We must note at this point that the exposure of the Cu and Sn species to open-circuit conditions under neutral pH, and the subsequent exposure to air when the samples are transferred to high vacuum, can create the oxidized states observed in the surface spectroscopy results. To unambiguously elucidate the chemical state of the catalyst, operando spectroscopic experiments are definitively required. Above all, we concluded that, during and after the electrochemical protocols, the Cu and Sn species are most likely in a zero-valence state, consistent with the standard redox potential expectations. This argument is in agreement with the XRD results, in which it was possible to observe the disappearance of bulk SnO_2 when steady-state electrocatalysis was performed for more than 14 h (Figure 6). XPS spectra of Cu 2p, O 1s and Sn 4d are shown in Figure S7 and Table S1, and the data are further discussed in the SI.

The drastic change in the product selectivity for alloying Cu-Sn leads to an important question on how the active site is altered between OD-Cu and Cu-Sn, which makes the electrode highly selective towards CO. The nature of the active site in Cu-Sn can be within a range of possibilities, which may include the formation of metallic Sn on the surface of metallic Cu or the formation of an alloy, based on the surface and bulk X-ray characterizations (Figures 6 and 7). It is reasonable to consider that Cu-Sn alloying leads to the suppression of the catalytic activity for H_2 without affecting the productivity towards CO (as observed in Figures 3 and 4). To test whether Sn is required for the selective generation of CO, we performed a control experiment in which OD-Cu was treated in the same solution of 2 M KOH without the presence of the $SnCl_2$

precursor salt. A very different electroreduction profile was obtained when compared with the plating step of the optimized Cu-Sn electrode (compare Figures S8 and S9a). The CO_2 reduction experiment at −0.6 V vs. RHE resulted in a much higher FE for H_2 (~35%) and HCOOH (~29%) (Figure S9b). It can be deduced from this result that Sn on Cu is required to achieve >90% FE towards CO as observed with the Cu-Sn sample (Figures 1, 3 and 4). To check the performance of a pure alloy, $Cu_{84}Sn_5$ powder derived electrode plate was characterized. XRD measurement (Figure S10) showed best match with a pure phase of alloy form $(Cu_{32}Sn)_{0.12}$ according to the literature.[59] The alloy was then tested for CO_2 reduction at −0.6 V vs. RHE, and only H_2 was generated (−0.15 mA cm^{-2}, Figure S10). The $Cu_{84}Sn_5$ alloy exhibited approximately half the current density for H_2 compared with OD-Cu at the same applied potential (compare Figures 1a and S10a). When OD-Cu was modified by electroplating the optimal amount of Sn, the H_2 activity exhibited a 4-fold decrease, making the Cu-Sn electrocatalyst more selective towards CO. The general observation in our experiments was that pristine metallic Sn and $Cu_{84}Sn_5$ (Figures S1 and S10) exhibited a high FE for H_2 with formate as a minor product at low to moderate potentials with low activity. At the other end, a pristine Cu metal and Sn electroplated in polycrystalline Cu both exhibited an H_2 FE of almost unity. Hence, we have systematically demonstrated that when changing the atomic composition from Cu to Cu-Sn to metallic Sn on Cu, only the precise modification of metallic Cu surfaces, which were derived from oxygen-rich samples, resulted in the efficient and selective electrocatalytic reduction of CO_2 to CO. More detailed in situ spectroscopic investigations are needed to elucidate the role of oxygen-rich metallic surfaces in the effective reduction of carbon dioxide.

DFT modeling

At this point, we have observed that flat Cu monometallic surfaces catalyze the electroreduction of water over CO_2 at potentials more positive than −0.8 V vs. RHE. Nevertheless, a rough Cu surface like the one generated after the electrochemical reduction of OD-Cu exhibited higher selectivity to reduce CO_2. Nanoparticle aggregates of Cu most likely compose the structure of such oxide-derived electrodes, which contain a higher density of highly unsaturated Cu atoms. Indeed, a size-dependent CO_2 reduction activity was described in the literature for Cu nanoparticles.[60] As the particle size decreases, the H_2 evolution activity increases accompanied by CO generation without the formation of hydrocarbons.[60] We have shown that decorating Cu with controlled amounts of Sn completely alters the CO_2 selectivity, generating CO with >90% FE. Hence, to elucidate the effect of Sn on rough Cu surfaces, we performed DFT calculations to study the preference of Sn when placed in a Cu nanoparticle (NP) to be embedded in the bulk or at the surface of a regular Cu structure (see details of the calculations in the Supporting Information and Figures S10-S12). Specifically, we performed cluster model calculations using a cluster of 55 Cu atoms with icosahedron symmetry (the icosahedron structure is more stable than the cuboctahedron structure by more than 3 eV), and we modeled a series of $Cu_{54}Sn$ clusters, with the Sn atom replacing a Cu atom of an icosahedron Cu_{55} at different positions, as shown in Figure 8. Further, since it is clear that a Cu_{55} NP is remarkably small, and has no well formed facets, we performed similar calculations under periodic boundary conditions using regular (100), (111) and (211) facets. Combining results from the Cu_{55} NP and the regular facets allows to achieve insights on the preference for Sn to replace Cu in the bulk, at regular surfaces, or at edges and corners, which is situations presenting low coordinated atoms.

Focusing on the Cu_{55} cluster, the Sn atom can be placed in four different sites. The best position corresponds to replace one Cu atom on the edge of the Cu_{55} NP, see Figure 8a. This geometry is followed (0.23 eV higher in energy) by that obtained by replacing one Cu at the corner of the icosahedron structure, Figure 8b. Moving the substitutional Sn atom inside the Cu_{55} NP results in clearly less stable geometries. In fact, replacing a Cu in the internal shell (an icosahedron with 12 equivalent atoms) is clearly disfavored (2.31 eV higher than the shell-edge geometry), and moving the Sn atom at the center of the Cu_{55} NP, Figure 8d, results highest in energy (2.93 eV higher than the best position).

Moving to the surface of Cu/Sn alloys, we modeled the effect of replacing one Cu atom with an Sn atom on a perfect Cu surface. Specifically, we considered the (100), (111) and (211) Cu facets. The first two facets are flat but have different atomic densities, with the highest on the (111) facet, and different binding sites: 4-fold and 3-fold sites on the (100) and (111) facets, respectively. The (211) facet is stepped, with 3 different types of Cu atoms, from highly saturated at the bottom of the step to highly unsaturated at the ridge of the step. Although we have clear evidence that with high Sn concentrations on the surface, the real alloys will result in surfaces that cannot be represented by a model consisting of a single Sn atom on a pure Cu surface, these models can still offer insights on local situations—i.e., if the Sn prefers to sit on flat surfaces, leaving the step sites to the Cu, or vice versa.

Optimization of the structures with a Sn atom replacing a surface Cu atom leads to a small geometrical deformation, with a small displacement of the Sn atom out of the (100) and (111) surfaces. This result is reasonable, considering the different atomic radii of Cu and Sn. From an energetics perspective, the relative substitution energy, E_{Sub}, which corresponds to the difference between the energy of substitution of a Cu atom in an inner layer (or the middle and

bottom atoms in the case of the (211) surface) with the energy of substitution of a Cu atom at the surface (or the Cu atom at the top of the ridge of the (211) surface) are reported in Figure 9. In conclusion, combining results from calculations on NP with those on regular surfaces, it emerges that Sn prefers to replace low coordinated Cu atoms, which means at the surface of regular surfaces or at edges and corners, rather than in layers below the surface.

Next, we investigated H and CO adsorption on the Cu (100) and (111) surfaces presenting an Sn atom, to have insights on the possible role of Sn in inhibiting H_2 production while preserving CO production capability. The electronic energy of free molecules was calculated as the electronic energy of the specific molecule, referring to graphene for the C atom, 1/2 H_2 for H atoms, and (H_2O-H_2) for O atoms. For adsorbed species, the electronic energy was calculated as the electronic energy of the relaxed slab/adsorbate species referring to the electronic energy of the relaxed clean slab, to graphene for the C atom, to 1/2 H_2 for H atoms, and to (H_2O-H_2) for O atoms.[37] The minimized geometries corresponding to H adsorption on the (100) facet of Cu are reported in Figure 10a to 10c, those corresponding to H adsorption on the (111) facet are reported in Figure S14. The analysis indicates that H adsorption in the middle of the hollow site, 4-fold and 3-fold on the (100) and (111) facets, respectively, is preferred over bridge adsorption between two Cu atoms and finally by adsorption on top of a single Cu atom.

In the second step, we calculated H adsorption on the same positions if an Sn atom is present as shown in Figure 10d to 10f for the (100) facet, in Figure S15 for the (111) facet. The result clearly shows that H does not bind to Sn on both the (100) and (111) facets, and the overall bonding of H to the (100) Sn-modified surface is reduced by 0.18 eV with respect to the bonding to the pure Cu structure of Figure 10a to 10c. In the most stable structures, the H atom is basically bridge coordinated to two Cu atoms, Figure 10e, or it is accommodated between three

Cu atoms, Figure 10d. H adsorption on the (111) Sn-modified surface is even more reduced, by 0.55 eV, since the 3-fold nature of the sites always enforces closer proximity to the weakly coordinating Sn atom (further details can be found in the SI).

Next, we considered CO coordination starting with CO adsorption on pure Cu, as shown in Figure 10 g to 10i for the (100) surface, see Figure S16 for the (111) surface. The reported energies indicate that CO adsorption on the Cu surface is substantially unselective: CO can bind to one Cu only, can bridge two Cu atoms, and can sit in the 4-fold site. We also investigated CO adsorption when an Sn atom is near the adsorption site on both the (100) and (111) surfaces, as shown in Figure 10j to 10l for the (100) surface and Figure S17 for the (111) surface. On both surfaces our calculations show that adsorption of CO is generally less affected than that of H by the presence of an Sn atom and that CO binding to the Cu distal to the Sn is the least affected as shown in Figure 10g to 10i. The reduced impact of Sn substitution on CO adsorption is clearly due to the strong adsorption of CO on top of a single Cu atom, whereas H clearly prefers coordination on a hollow site, which is the site most perturbed by the presence of a Sn atom. Incidentally, we were unable to find CO coordinated to the 4-fold site because the geometry optimizations collapsed into the structure as shown in Figure 10j to 10l. In short, the analysis suggests that an Sn atom perturbs profoundly the multi-fold site on the surface of pure Cu, disfavoring adsorbed H in particular. We believe that these results on the (100) and (111) facets can be extended to any multi-fold sites on any facets, kinks, and edges.

Based on the previous observations, we can reasonably consider that as we modified the Cu^0 surface with Sn^0, we selectively diminished the competitive reaction rate for water reduction. We may suggest that as the alloy forms in the surface under the studied cathodic conditions, the H_2 activity exhibited a 4-fold reduction, leading to a decrease in the overall

activity of the Cu-Sn electrode. The $Cu_{84}Sn_5$ alloy indicated that only H_2 was generated under the investigated potential range; hence, Cu sites with preference for the formate-making mechanism may be competitive to H-binding sites that are inhibited by the introduction of Sn atoms. At the end, the catalysis of CO_2 reduction to CO seems unperturbed, creating highly selective sites by the systematic modification of the oxygen-rich metallic Cu surface.

As for a comparison between Cu-Sn in the current study and Cu-In in our previous study,[24,25] the two catalysts have similar behavior towards CO_2 electro-reduction: i.e., high selectivity towards CO evolution. DFT calculation shows preferential substitution at the top of the ridge on the (211) facet, destabilization of H adsorption on the flat (100) facet.[24,25] However, Bader charge analysis indicates that In transfers a slightly higher amount of electrons to the surrounding Cu atoms. For example, on the (100) facet the Bader charge of In is +0.33e, while the Bader charge on Sn is +0.22e. This result is in line with the electronegativity trend, Sn/1.96 > In/1.78, on the Pauling electronegativity scale. Overall, although some difference in electronic structure preference between Cu-Sn and Cu-In was obtained, it is considered that the improvement in FE for CO originates from the common cause: reduction of the capability of hydrogen adsorption, which in turn enhances the selectivity exclusively to CO.

4. Conclusions

The Sn electrodeposited on OD-Cu electrocatalyst conserves a high selectivity to make CO from CO_2 (>90% FE) over a wide potential range (−0.4 to −0.8 V vs. RHE) for long period of time (at least 14 h). The elemental analysis of the Cu-Sn electrode showed a CO selectivity dependence on deposited amounts of Sn. The bimetallic Cu-Sn electrocatalyst with an optimal composition efficiently and selectively generates CO from the reduction of aqueous CO_2 while

the monometallic Cu promotes H_2 evolution. Excess Sn deposited on reduced OD-Cu also diminished the CO FE while favoring H_2 generation with a low current density. From XRD, a Cu-Sn alloy formed after 14 h of steady-state CO_2 reduction. Cu LMM Auger spectra indicated the existence of Cu^0 in the surface after the electroplating of Sn and after the electrocatalytic reaction. DFT calculations show a decrease in the adsorption of H when atomic Sn replaces Cu, supporting the experimental data on the observed low selectivity for H_2 on the Cu-Sn electrocatalyst. Our results suggest that Sn substitutes Cu^0 on the surface of reduced OD-Cu, leading to the formation of a Cu-Sn structure. As the formation of adsorbed H* was inhibited, the energetics to form H_2 and to bind the COOH* intermediate would have been perturbed as well, hindering the H_2 and formate generation mechanism. Nonetheless, the sites favoring the binding of CO were mostly unchanged. Further work should focus on *operando* spectroscopic characterizations to elucidate the exact structure of active sites and the role of subsurface oxygen impurities during the aqueous electrocatalytic reduction of CO_2. Our approach provides an example in which employing low-cost, non-noble metals produces a highly selective bimetallic electrocatalyst for the scalable electrochemical reduction of CO_2.

ASSOCIATED CONTENT

The Supporting Information describes the following contents: Electrodeposition profile of Sn deposited on OD-Cu. Electrochemical performance of Sn metal. Electrochemical performance of OD-Cu reduced without Sn. Electrochemical performance of $Cu_{32}Sn$ alloy. Effect of electrodeposited charge on product selectivity. Electrochemical comparison of OD-Cu synthesized via different procedures. Further analysis and procedure on DFT calculations. This material is available free of charge via the Internet at http://pubs.acs.org.

AUTHOR INFORMATION

Corresponding Author

*Kazuhiro Takanabe, E-mail: kazuhiro.takanabe@kaust.edu.sa

Author Contributions

The manuscript was written through contributions of all authors. All authors have given approval to the final version of the manuscript. ‡S.S. and A.-T.G.-E. contributed equally.

ACKNOWLEDGMENT

The research reported in this publication was supported by King Abdullah University of Science and Technology (KAUST). Furthermore, we are also thankful to Dr. Shahid Rasul at KAUST for the helpful discussions. We are also grateful for the computational resources acquired from KAUST Supercomputing Laboratory using the supercomputer Shaheen II under the project k1016.

ABBREVIATIONS

DFT, Density Functional Theory; FE, Faradaic Efficiency; μGC, micro Gas Chromatography; HPLC, High-Performance Liquid Chromatography; ICP, Inductively Coupled Plasma; OD-Cu, Oxide-derived Copper; SEM, Scanning Electron Microscopy; XRD, X-ray Diffraction; XPS, X-ray photoelectron spectroscopy.

REFERENCES

1. Appel, A. M.; Bercaw, J. E.; Bocarsly, A. B.; Dobbek, H.; DuBois, D. L.; Dupuis, M.; Ferry, J. G.; Fujita, E.; Hille, R.; Kenis, P. J.; Kerfeld, C. A.; Morris, R. H.; Peden, C. H.; Portis,

A. R.; Ragsdale, S. W.; Rauchfuss, T. B.; Reek, J. N.; Seefeldt, L. C.; Thauer, R. K.; Waldrop, G. L. *Chem. Rev.* **2013,** *113*, 6621-6658.

2. Ozin, G. A. *Adv. Mater.* **2015,** *27*, 1957-1963.

3. Agarwal, A. S.; Zhai, Y.; Hill, D.; Sridhar, N. *ChemSusChem* **2011,** *4*, 1301-1310.

4. Spinner, N. S.; Vega, J. A.; Mustain, W. E. *Catal. Sci. Technol.* **2012,** *2*, 19-28.

5. Kauffman, D. R.; Thakkar, J.; Siva, R.; Matranga, C.; Ohodnicki, P. R.; Zeng, C.; Jin, R. *ACS Appl. Mater. Inter.* **2015,** *7*, 15626-15632.

6. Chen, Y.; Li, C. W.; Kanan, M. W. *J. Am. Chem. Soc.* **2012,** *134*, 19969-19972.

7. Min, X.; Kanan, M. W. *J. Am. Chem. Soc.* **2015,** *137*, 4701-4708.

8. Lu, Q.; Rosen, J.; Zhou, Y.; Hutchings, G. S.; Kimmel, Y. C.; Chen, J. G.; Jiao, F. *Nat. Commun.* **2014,** *5*, 3242.

9. Hahn, C.; Abram, D. N.; Hansen, H. A.; Hatsukade, T.; Jackson, A.; Johnson, N. C.; Hellstern, T. R.; Kuhl, K. P.; Cave, E. R.; Feaster, J. T.; Jaramillo, T. F. *J. Mater. Chem. A* **2015,** *3*, 20185-20194.

10. Kortlever, R.; Peters, I.; Koper, S.; Koper, M. T. M. *ACS Catal.* **2015**, *5*, 3916-3923.

11. Hori, Y.; Murata, A.; Takahashi, R. *J. Chem. Soc., Farad. Trans. 1* **1989,** *85*, 2309-2326.

12. Li, C. W.; Kanan, M. W. *J. Am. Chem. Soc.* **2012,** *134*, 7231-7234.

13. Hori, Y. Electrochemical CO_2 Reduction on Metal Electrodes. In *Modern Aspects of Electrochemistry*, Vayenas, C.; White, R.; Gamboa-Aldeco, M., Eds. Springer New York: 2008; Vol. 42, pp 89-189.

14. Verdaguer-Casadevall, A.; Li, C. W.; Johansson, T. P.; Scott, S. B.; McKeown, J. T.; Kumar, M.; Stephens, I. E.; Kanan, M. W.; Chorkendorff, I. *J. Am. Chem. Soc.* **2015,** *137*, 9808-9811.

15. Garcia-Esparza, A. T.; Limkrailassiri, K.; Leroy, F.; Rasul, S.; Yu, W.; Lin, L.; Takanabe, K. *J. Mater. Chem. A* **2014,** *2*, 7389-7401.

16. Xiao, J.; Kuc, A.; Frauenheim, T.; Heine, T. *J. Mater. Chem. A* **2014,** *2*, 4885-4889.

17. Lee, C. H.; Kanan, M. W. *ACS Catal.* **2015,** *5*, 465-469.

18. Asadi, M.; Kumar, B.; Behranginia, A.; Rosen, B. A.; Baskin, A.; Repnin, N.; Pisasale, D.; Phillips, P.; Zhu, W.; Haasch, R.; Klie, R. F.; Kral, P.; Abiade, J.; Salehi-Khojin, A. *Nat. Commun.* **2014**, *5*, 4470.

19. DiMeglio, J. L.; Rosenthal, J. *J. Am. Chem. Soc.* **2013**, *135*, 8798-8801.

20. Medina-Ramos, J.; DiMeglio, J. L.; Rosenthal, J. *J. Am. Chem. Soc.* **2014**, *136*, 8361-8367.

21. Medina-Ramos, J.; Pupilo, R. C.; Keane, T. P.; DiMeglio, J. L.; Rosenthal, J. *J. Am. Chem. Soc.* **2015**, *137*, 5021-5027.

22. Hansen, H. A.; Varley, J. B.; Peterson, A. A.; Norskov, J. K. *J. Phys. Chem. Lett.* **2013,** *4*, 388-392.

23. Peterson, A. A.; Nørskov, J. K. *J. Phys. Chem. Lett.* **2012,** *3*, 251-258.

24. Rasul, S.; Anjum, D. H.; Jedidi, A.; Minenkov, Y.; Cavallo, L.; Takanabe, K. *Angew. Chem. Int. Ed.* **2015,** *54*, 2146-2150.

25. Jedidi, A.; Rasul, S.; Masih, D.; Cavallo, L.; Takanabe, K. *J. Mater. Chem. A* **2015,** *3*, 19085-19092.

26. Watanabe, M.; Shibata, M.; Kato, A.; Azuma, M.; Sakata, T. *J. Electrochem. Soc.* **1991,** *138*, 3382-3389.

27. Hori, Y.; Wakebe, H.; Tsukamoto, T.; Koga, O. *Electrochim. Acta* **1994,** *39*, 1833-1839.

28. Won, D. H.; Choi, C. H.; Chung, J.; Chung, M. W.; Kim, E.-H.; Woo, S. I. *ChemSusChem* **2015,** *8*, 3092-3098.

29. Chen, Y.; Kanan, M. W. *J. Am. Chem. Soc.* **2012,** *134*, 1986-1989.

30. Greeley, J.; Jaramillo, T. F.; Bonde, J.; Chorkendorff, I. B.; Norskov, J. K. *Nat. Mater.* **2006,** *5*, 909-913.

31. Trasatti, S. *J. Electroanal. Chem. Interfacial Electrochem.* **1972,** *39*, 163-184.

32. Miller, D. J.; Biesinger, M. C.; McIntyre, N. S. *Surf. Interface Anal.* **2002,** *33*, 299-305.

33. Kresse, G.; Furthmüller, J. *Phys. Rev. B* **1996,** *54*, 11169-11186.

34. Kresse, G.; Hafner, J. *Phys. Rev. B* **1993,** *47*, 558-561.

35. Kresse, G.; Hafner, J. *Phys. Rev. B* **1994,** *49*, 14251-14269.

36. Kresse, G.; Hafner, J. *Mater. Sci.* **1996,** *6*, 15-50.

37. Peterson, A. A.; Abild-Pedersen, F.; Studt, F.; Rossmeisl, J.; Norskov, J. K. *Energy Environ. Sci.* **2010,** *3*, 1311-1315.

38. Blöchl, P. E. *Phys. Rev. B* **1994,** *50*, 17953-17979.

39. Kresse, G.; Joubert, D. *Phys. Rev. B* **1999,** *59*, 1758-1775.

40. Muñoz, J. A.; Lucas, M. S.; Mauger, L.; Halevy, I.; Horwath, J.; Semiatin, S. L.; Xiao, Y.; Chow, P.; Stone, M. B.; Abernathy, D. L.; Fultz, B. *Phys. Rev. B* **2013,** *87*, 014301.

41. von Pezold, J.; Dick, A.; Friák, M.; Neugebauer, J. *Phys. Rev. B* **2010,** *81*, 094203.

42. Ramos de Debiaggi, S.; Deluque Toro, C.; Cabeza, G. F.; Fernández Guillermet, A. *J. Alloys Compd.* **2012,** *542*, 280-292.

43. Jedidi, A.; Markovits, A.; Minot, C.; Abderrabba, M. *Chem. Phys. Lett.* **2012,** *541*, 101-104.

44. Jedidi, A.; Markovits, A.; Minot, C.; Abderrabba, M.; Van Hove, M. A. *Phys. Chem. Chem. Phys.* **2014,** *16*, 20703-20713.

45. Ren, D.; Deng, Y.; Handoko, A. D.; Chen, C. S.; Malkhandi, S.; Yeo, B. S. *ACS Catal.* **2015,** *5*, 2814-2821.

46. Kim, S. M.; Hsu, A.; Lee, Y.-H.; Dresselhaus, M.; Palacios, T.; Kim, K. K.; Kong, J. *Nanotechnology* **2013,** *24*, 365602.

47. Kim. Y.-G.; Baricuatro, J. H.; Javier, A.; Gregoire, J. M.; Soriaga, M. P. *Langmuir* **2014**, *30*, 15053-15056.

48. Paracchino, A.; Laporte, V.; Sivula, K.; Gratzel, M.; Thimsen, E. *Nat. Mater.* **2011,** *10*, 456-461.

49. Larson, P. E. *J. Electron. Spectrosc.* **1974,** *4*, 213-218.

50. Haber, J.; Machej, T.; Ungier, L.; Ziółkowski, J. *J. Solid State Chem.* **1978,** *25*, 207-218.

51. McIntyre, N. S.; Sunder, S.; Shoesmith, D. W.; Stanchell, F. W. *J. Vac. Sci. Technol.* **1981,** *18*, 714-721.

52. Poulston, S.; Parlett, P. M.; Stone, P.; Bowker, M. *Surf. Interface Anal.* **1996,** *24*, 811-820.

53. Chawla, S. K.; Sankarraman, N.; Payer, J. H. *J. Electron Spectrosc. Relat. Phenom.* **1992,** *61*, 1-18.

54. Chawla, S. K.; Rickett, B. I.; Sankarraman, N.; Payer, J. H. *Corros. Sci.* **1992,** *33*, 1617-1631.

55. Iijima, J.; Lim, J. W.; Hong, S. H.; Suzuki, S.; Mimura, K.; Isshiki, M. *Appl. Surf. Sci.* **2006,** *253*, 2825-2829.

56. Speckmann, H. D.; Haupt, S.; Strehblow, H. H. *Surf. Interface Anal.* **1988,** *11*, 148-155.

57. Hegde, R. I.; Sainkar, S. R.; Badrinarayanan, S.; Sinha, A. P. B. *J. Electron. Spectrosc.* **1981,** *24*, 19-25.

58. Kövér, L.; Kovács, Z.; Sanjinés, R.; Moretti, G.; Cserny, I.; Margaritondo, G.; Pálinkás, J.; Adachi, H. *Surf. Interface Anal.* **1995,** *23*, 461-466.

59. Kambolov, D. A.; Kashezhev, A. Z.; Kutuev, R. A.; Korotkov, P. K.; Manukyants, A. R.; Ponezhev, M. Kh.; Sozaev, V. A. *J. Surf. Investig. X-RA.* **2015**, *9*, 636-640.

60. Reske, R.; Mistry, H.; Behafarid, F.; Roldan Cuenya, B.; Strasser, P. *J. Am. Chem. Soc.* **2014,** *136*, 6978-6986.

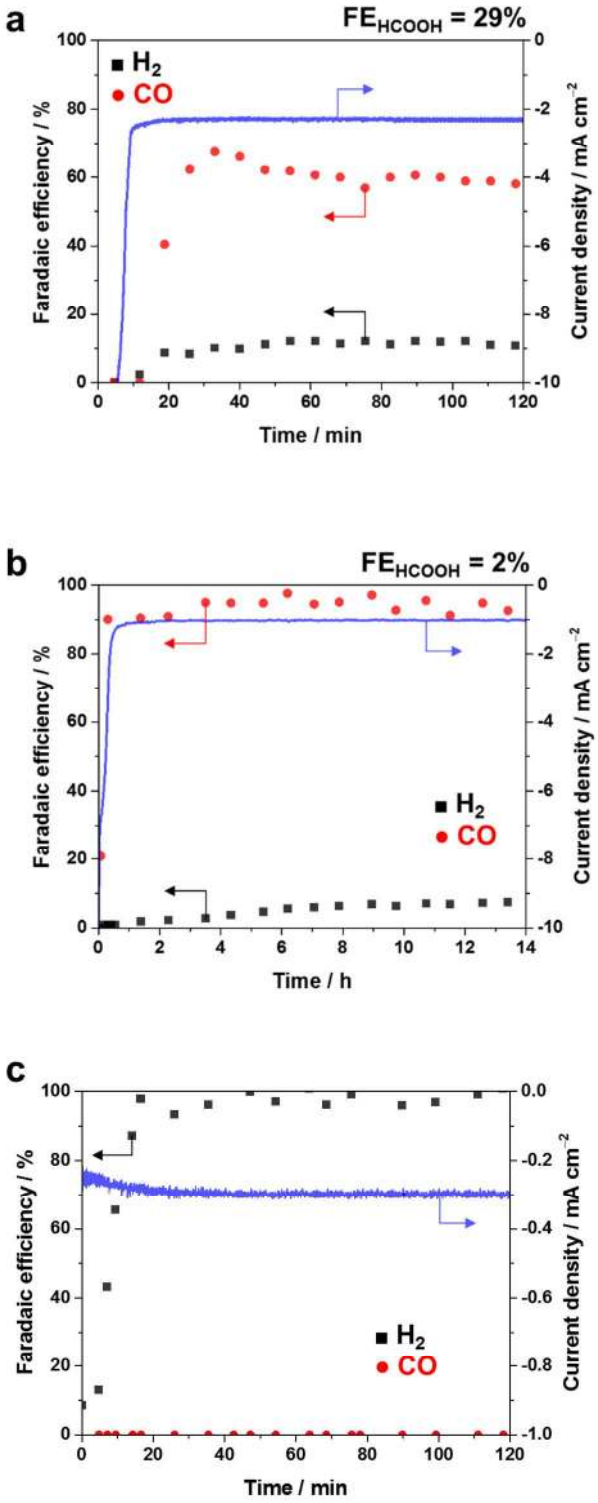

Figure 1. Gas chromatograph product analysis for (a) OD-Cu, (b) Cu-Sn (14 h) and (c) Sn deposited on Sn at −0.6 V vs. RHE in 0.1 M $KHCO_3$ (pH 6.8) saturated with CO_2.

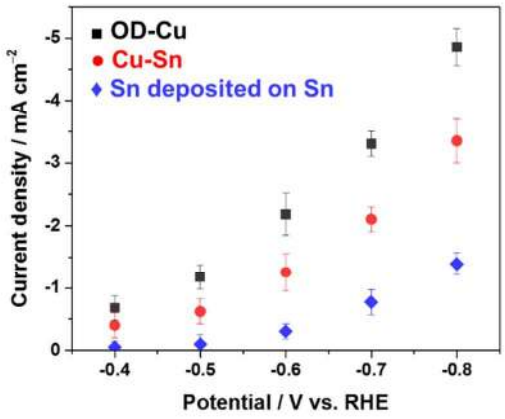

Figure 2. Current density comparison among OD-Cu, Cu-Sn, and Sn deposited on Sn (0.1 M $KHCO_3$, pH 6.8, saturated CO_2).

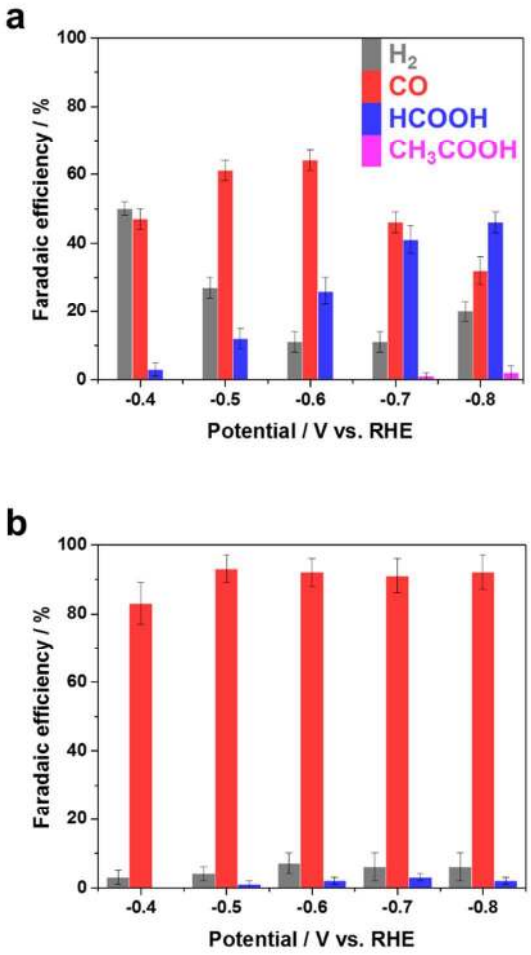

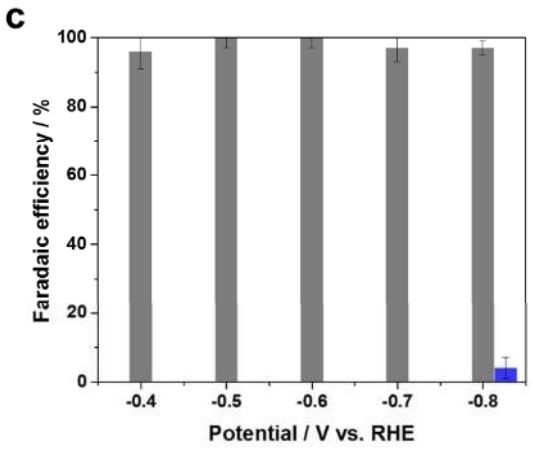

Figure 3. Faradaic efficiency analysis of (a) OD-Cu (b) Cu-Sn and (c) Sn deposited on Sn sheet at applied potentials (0.1 M $KHCO_3$, pH 6.8, saturated CO_2). The Faradaic efficiency is stated as an average and calculated at the steady-state current and product concentration.

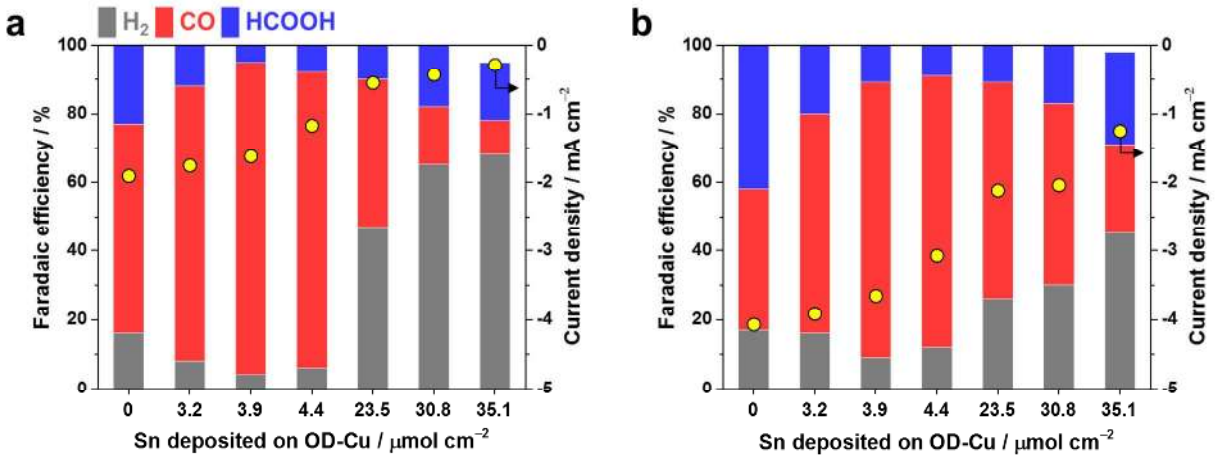

Figure 4. Effect of Sn deposition amount on the pre-reduced OD-Cu on CO_2 electroreduction performance at (a) −0.6 V and at (b) −0.8 V vs. RHE in 0.1 M $KHCO_3$ (pH 6.8) saturated with CO_2. The circles represent steady-state current densities.

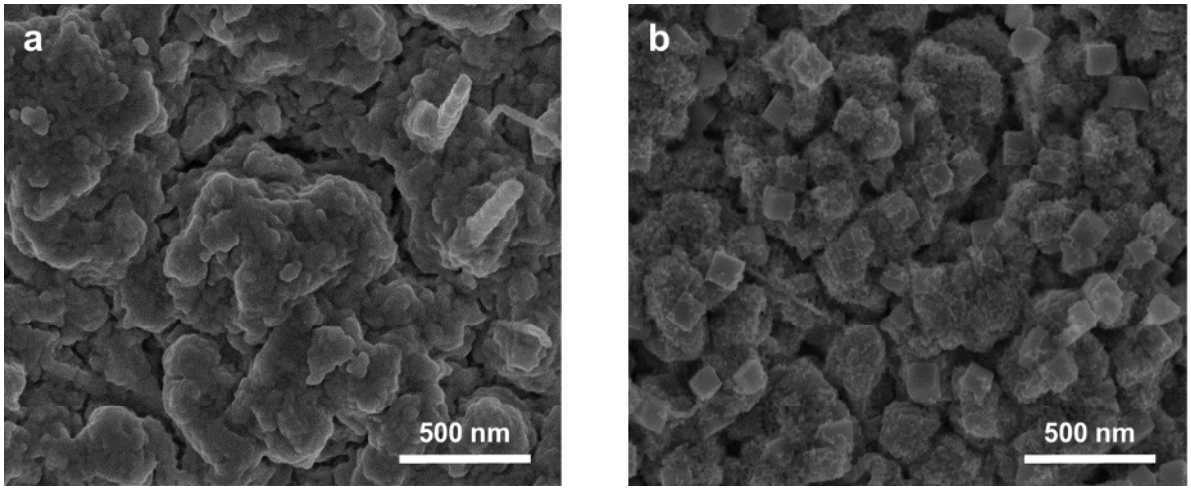

Figure 5. SEM images of (a) Cu-Sn before CO_2 reduction, (b) Cu-Sn after 1 h of CO_2 reduction at −0.6 V vs. RHE.

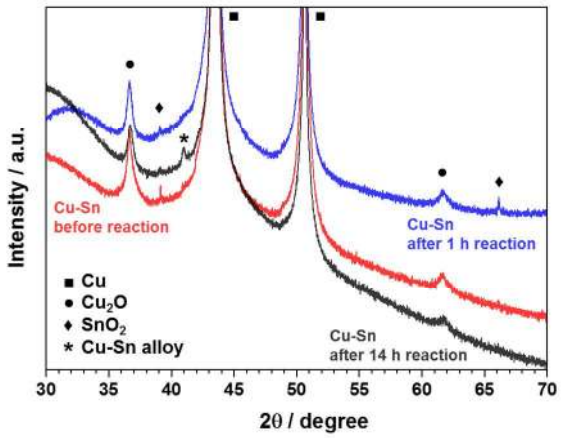

Figure 6. XRD patterns of Cu-Sn before and after 1 h of CO_2 reduction, and after 14 h CO_2 reduction at −0.6 V vs. RHE.

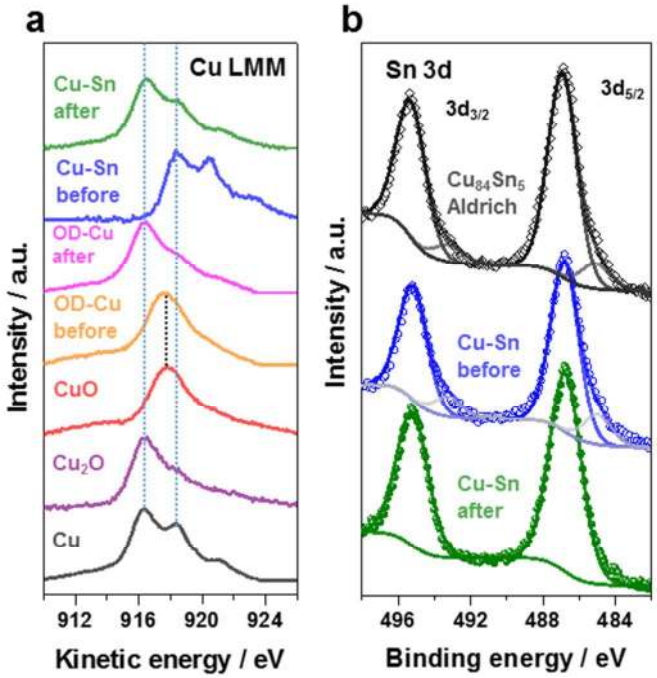

Figure 7. (a) Cu $L_3M_{45}M_{45}$ Auger spectra and (b) XPS Sn 3d spectra for OD-Cu and Cu-Sn samples before and after CO_2 electrocatalysis. Reference spectra from standard samples are also shown for comparison.

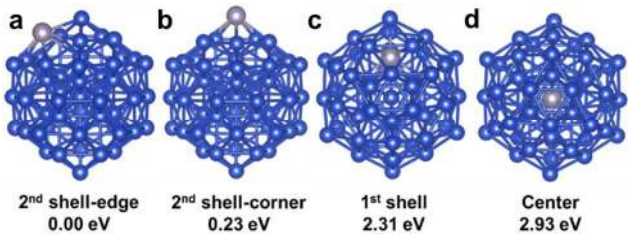

Figure 8. All possible positions of an Sn atom replacing a Cu atom on a Cu_{55} structure to form a $Cu_{54}Sn$ structure: (a) 2nd shell-edge, (b) 2nd shell-corner, (c) 1st shell, and (d) center of a C_{55} nanoparticle.

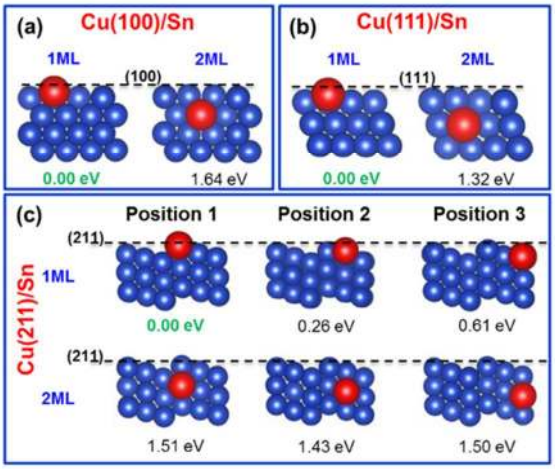

Figure 9. Side view of the (a) (100), (b) (111) and (c) (211) facets of fcc copper crystal with the replacement of one Cu atom by an Sn atom from the top or the second layer. The relative substitution energy, E_{Sub}, is reported in eV.

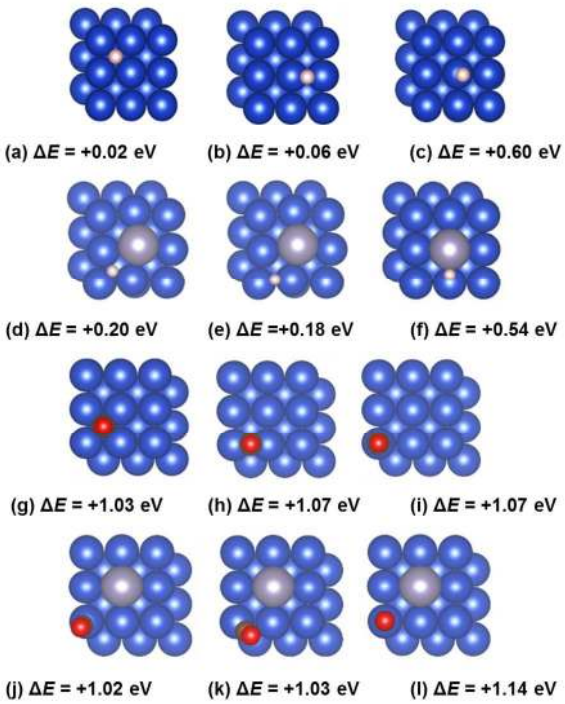

Figure 10. Optimized geometries and relative energies of **(a, b, c)** H adsorbed on the Cu(100) facet. ΔE is the electronic energy of the state minus the electronic energy of the clean slab

associated with that state, with the H atom referenced to 1/2 H_2 **(d, e, f)** H adsorbed on the Sn-modified Cu(100) facet. ΔE is the electronic energy of the state minus the electronic energy of the clean slab associated with that state, with the H atom referenced to 1/2 H_2 **(g, h, i)** CO adsorbed on the (100) Cu facet. ΔE is the electronic energy of the state minus the electronic energy of the clean slab associated with that state, with the C atom referenced to graphene and the O atom to (H_2O-H_2) **(j, k, l)** H adsorbed on the Sn-modified (100) Cu facet. ΔE is the electronic energy of the state minus the electronic energy of the clean slab associated with that state, with the C atom referenced to graphene and the O atom to (H_2O-H_2).

Insert Table of Contents Graphic and Synopsis Here